Research Square

Preprints are preliminary reports that have not undergone peer review.
They should not be considered conclusive, used to inform clinical practice,
or referenced by the media as validated information.

Achieving Diagnostic-Quality Rapid PSMA PET Across Scanners and Tracers with a Generative Adversarial Network

Chao Cheng
Changhai Hospital
Boyang Pan
Shanghai Key Laboratory of Magnetic Resonance, School of Physics, East China Normal University
Langdi Zhong
RadioDynamic Medical
Libo Xu
Tsinghua Cross-Strait Research Institute
Zhongqiu Guo
Changhai Hospital
Qinqin Yang
Changhai Hospital
Guixia Pan
Changhai Hospital
Siyu Liang
Changhai Hospital
Nanjie Gong
nanjie.gong@gmail.com

Shanghai Key Laboratory of Magnetic Resonance, School of Physics, East China Normal University
Changjing Zuo
Changhai Hospital

Research Article

Keywords: PSMA PET, Generative Adversarial Network(GAN), Accelerated Imaging, Prostate Cancer, Image Enhancement

Posted Date: May 4th, 2026

DOI: https://doi.org/10.21203/rs.3.rs-9338733/v1

License: This work is licensed under a Creative Commons Attribution 4.0 International License.
Read Full License

Additional Declarations: No competing interests reported.

Abstract

Background: To evaluate the performance of a Channel Dense Dense U-Generative Adversarial Network (CDDU-GAN), in restoring the quality of four-fold accelerated Prostate-Specific Membrane Antigen (PSMA) PET acquisitions across different radiotracers and hybrid imaging platforms.

Methods: This prospective study enrolled 84 patients who underwent either 18F-PSMA or 68Ga-PSMA PET imaging on PET/CT or PET/MR systems. Standard-dose listmode data (120s/bed for PET/CT, 240s/bed for PET/MR) were retrospectively subsampled to simulate a rapid-scan protocol (30s/bed and 60s/bed, respectively). The CDDU-GAN was trained to transform these low-count images to a quality equivalent to the standard-dose acquisitions. Objective image quality was quantified using Peak Signal-to-Noise Ratio (PSNR) and Structural Similarity Index (SSIM). Subjective image quality was independently assessed by two blinded nuclear medicine physicians using a 5-point Likert scale for overall quality, lesion conspicuity, and diagnostic confidence. Statistical significance was determined using the Wilcoxon signed-rank test.

Results: The CDDU-GAN framework yielded significant improvements in objective quality for the total cohort, increasing the mean PSNR from 46.8±7.5 to 48.2±6.6 ($p<0.0001$) and SSIM from 0.980±0.026 to 0.986±0.020 ($p<0.0001$). Performance gains were more pronounced for PET/CT datasets (PSNR increase: +3.3 dB for 18F-PSMA; +2.5 dB for 68Ga-PSMA) than for PET/MR. Inter-rater reliability for subjective analysis was substantial to almost perfect. The CDDU-GAN-enhanced images received significantly higher scores than unprocessed fast-scan images across all subjective metrics ($p<0.05$). Notably, the model increased the mean diagnostic confidence score for the entire cohort from 3.37±1.27 to 3.78±1.22, substantially closing the gap to the standard-dose score of 4.22±1.23 and restoring diagnostic utility in challenging cases.

Conclusion: The proposed CDDU-GAN framework effectively restores image quality and diagnostic confidence in four-fold accelerated PSMA PET imaging. By successfully mitigating noise and improving image fidelity across different tracers and platforms, this deep learning approach holds significant potential to increase patient throughput, reduce motion artifacts, and improve patient comfort without a critical loss of diagnostic information.

Introduction

Prostate-specific membrane antigen (PSMA) PET imaging has become a vital modality in the early diagnosis and staging of prostate cancer, providing precise visualization of tumor spread, even at low volumes.[1, 2]. Current clinical practice primarily employs radiotracers labeled with Gallium-68 (68Ga-PSMA) or Fluorine-18 (18F-PSMA), which exhibit distinct physical and biological characteristics, including half-life, positron energy, imaging resolution, and tracer kinetics [3]. 68Ga-PSMA PET/CT has consistently demonstrated high sensitivity and specificity for prostate cancer detection [4], whereas 18F-labeled PSMA ligands offer improved spatial resolution, enhanced image quality, and more favorable logistical and economic profiles due to their longer half-life [5, 6]. Owing to the intrinsic spatial resolution

limitations of PET, hybrid imaging approaches such as PET/CT and PET/MR provide superior anatomical correlation and contribute to improved diagnostic accuracy, thereby facilitating more precise risk stratification and clinical decision-making in prostate cancer management [7, 8].

Accelerated imaging techniques substantially enhance scanning efficiency by markedly reducing acquisition time, thereby improving scanner utilization. Shortened scan duration also contributes to improved patient experience, particularly benefiting pediatric, elderly, and other populations who may have difficulty maintaining prolonged immobility. From a clinical perspective, accelerated imaging facilitates more rapid availability of diagnostic information, which supports timely therapeutic decision-making and may ultimately improve patient outcomes.[9] In PET/CT and PET/MRI, accelerated acquisition protocols may lead to a reduction in temporal resolution, particularly in the presence of physiological motion such as respiration or cardiac activity [10]. Such limitations can adversely affect the accuracy of attenuation correction [11], thereby contributing to an increased risk of imaging artifacts.

Recent advances in deep learning (DL), particularly generative adversarial networks (GANs), have shown promise in reconstructing high-quality PET images from ultra-low-dose or accelerated acquisitions [12, 13]. In fluorodeoxyglucose (FDG) PET, DL-based methods have successfully generated diagnostically reliable images with reduced scan times and lower radiation exposure [14]. However, PSMA-based PET presents unique challenges: accelerated protocols often yield fewer counts and lower signal-to-noise ratios (SNR) than FDG based, which affects the diagnosis of early recurrence or metastasis of prostate cancer [15, 16]. In previous work, GAN-based methods such as CycleGAN have been applied to translate low-dose PET into full-dose equivalents with improvements in structural similarity [17, 18], while convolutional neural networks (CNNs), including 3D U-Nets, have demonstrated efficacy in preserving small lesion visibility but often lack global contextual awareness [19, 20]. More recently, hybrid architectures integrating CNNs with attention mechanisms or transformer modules have been explored to enhance feature representation across scanners and protocols [21, 22]. In the specific context of PSMA PET, deep supervised residual U-Nets have achieved promising results in multi-center PET/CT reconstruction [23]. Nevertheless, existing approaches generally fail to fully exploit inter-slice channel dependencies and often struggle to suppress the high-granularity noise patterns that are characteristic of accelerated PSMA acquisitions.

To address these limitations, this study aims to evaluate the performance of a deep learning-based image enhancement framework across diverse clinical scenarios. Our primary objective is to compare its impact on image quality and diagnostic efficiency for acquisitions using two key PSMA tracers (68Ga-PSMA and 18F-PSMA) on two major imaging platforms (PET/MR and PET/CT). To achieve this, we employ an advanced model based on a Generative Adversarial Network (GAN), which incorporates a Channel Dense Dense U-GAN (CDDU-GAN) with embedded channel attention mechanisms, to validate its robustness and potential under complex clinical conditions.

Materials and Methods

2.1 Dataset acquisition

This prospective study was approved by the Institutional Review Board of Shanghai Changhai Hospital in accordance with the Declaration of Helsinki. Written informed consent was obtained from all patients. A total of 84 patients with known or suspected prostate cancer were enrolled between December 2020 and January 2024. The patient cohort had a mean age of 67.6 ± 7.8 years. The mean body weight was 69.1 ± 9.9 kg. The study population was divided into four cohorts based on the radiotracer and imaging modality used: (1) 19 cases of 18F-PSMA PET-CT (FPC); (2) 15 cases of 18F-PSMA PET-MR (FPM); (3) 9 cases of 68Ga-PSMA PET-CT (GaPC); (4) 41 cases of 68Ga-PSMA PET-MR (GaPM).

All PET/CT examinations were performed on a Biograph 64 PET/CT scanner (Siemens Healthcare, Erlangen, Germany), and PET/MR examinations were conducted on a Biograph mMR scanner with 3.0T MRI system(Siemens Healthcare, Erlangen, Germany). Patients received a single, slow intravenous bolus injection of the radiotracer. For the 68Ga-PSMA cohorts, the administered activity was weight-adjusted, ranging from 2.00 to 2.50 MBq/kg. For the 18F-PSMA cohorts, the administered activity ranged from 3.00 to 3.33 MBq/kg. Following injection, patients underwent a standard radiotracer uptake period. Image acquisition commenced at 45–60 minutes post-injection for patients receiving 68Ga-PSMA, and at 90–120 minutes post-injection for patients receiving 18F-PSMA, corresponding to the respective optimal tumor-to-background contrast windows for these tracers.

Standard-dose (full-time) acquisitions were acquired in listmode for 120 seconds per bed position for PET/CT and 240 seconds per bed position for PET/MR. To simulate a rapid acquisition protocol, the listmode data was uniformly subsampled to one-fourth of the total counts, corresponding to effective scan times of 30 seconds for PET/CT and 60 seconds for PET/MR.

Both standard-dose and simulated rapid-scan listmode data were reconstructed using a Ordered Subsets Expectation Maximization (OSEM) algorithm with [Number] iterations and [Number] subsets. The reconstruction included corrections for [e.g., attenuation, scatter, randoms, and detector normalization]. The final images were reconstructed into a matrix of 128x128. A post-reconstruction Gaussian filter with a full width at half maximum (FWHM) of [e.g., 4.0 mm] was applied.

The acquired datasets were partitioned into training and testing sets for the development and evaluation of our deep learning model. The FPC cohort was split into 9 training and 10 testing cases. The FPM cohort was divided into 8 training and 7 testing cases. The GaPM cohort consisted of 24 training and 17 testing cases. The entire GaPC cohort of 9 cases was reserved exclusively for testing to assess the model's generalization capabilities on an independent dataset.

2.2 Deep Learning Method

The Channel Dense Dense U-GAN(CDDU-GAN) proposed in this study is an improvement of DDUNet[25] with channel attention mechanisms and adversarial generative loss. The general structureof CDDU-GAN was shown in Fig. 1. Unlike U-Net's isolated feature propagation between encoder-decoder pairs, DDUNet

establishes cross-U-Net dense connections at every scale level, enabling comprehensive gradient flow and feature reuse across cascaded U-Net blocks. The dual-dense mechanism—combining local residual dense blocks with global feature fusion—enhances texture preservation and edge recovery, particularly in high-noise scenarios.

To address the unique challenges of multi-tracer PET image denoising, we enhanced the foundational DDUNet architecture with two synergistic mechanisms designed to improve both model adaptability and the perceptual quality of the output.

First, we introduced a Channel Attention (CA) module strategically integrated within each encoding and decoding block of the UNet architecture. The purpose of the CA module is to enable adaptive feature recalibration. By dynamically modulating the weights of different feature channels based on the input data, the network learns to emphasize the most informative features while suppressing irrelevant ones. This is particularly critical in a multi-tracer setting, where ^68Ga-PSMA and ^18F-PSMA exhibit distinct noise characteristics and signal distributions. The CA mechanism empowers the model to create a unified and robust denoising pipeline that is intrinsically sensitive to these tracer-specific variations without requiring separate models.

Second, to overcome the inherent smoothing effect of conventional pixel-wise loss functions (e.g., L1 or MSE) and to generate images with higher diagnostic fidelity, we incorporated a sophisticated adversarial training scheme. This scheme employs a UNet-based discriminator, which deviates from standard discriminators by providing localized, patch-level feedback on image realism rather than a single global validity score. By training the generator against this advanced discriminator, we compel it to produce images with high-frequency details and textures that are perceptually indistinguishable from full-dose, low-noise ground truth images. This is crucial for preserving the subtle yet diagnostically critical features of tracer uptake, such as the texture of small lesions, which might otherwise be averaged out. The total loss of the network can be expressed as follow:

$$Loss_{total} = \gamma_1 \times Loss_{mse} + \gamma_2 \times Loss_{ssim} + \gamma_3 \times Loss_{adv}$$

where $\mathrm{Loss}_{\mathrm{mse}}$ is the mean square error loss, $\mathrm{Loss}_{\mathrm{ssim}}$ is the structure similarity index loss, and $\mathrm{Loss}_{\mathrm{adv}}$ is the adversarial generative loss. γ_1, γ_2, and γ_3 are 1, 0.2, 0.05 respectively.

The network was trained using the Adam optimizer due to its proven efficacy in handling the complex, high-dimensional optimization landscapes typical of generative models. We utilized the default parameters for the optimizer (β_1 = 0.9, β_2 = 0.999). All weights in the generator and discriminator networks were initialized from a Gaussian distribution with a mean of 0 and a standard deviation of 0.02 to break symmetry and promote effective learning from the start.

Our training was conducted for a total of 200 epochs using a batch size of 10. To ensure stable convergence and prevent mode collapse, we adopted a two-phase training strategy:

1. Generator Pre-training: For the initial 50 epochs, the generator was trained in isolation, optimized solely on a pixel-wise loss (e.g., L1 Mean Absolute Error). This "warm-up" phase allows the generator to learn the fundamental mapping from low-dose to high-dose images and reach a stable, reasonable state before the introduction of the more complex adversarial objective.
2. Full Adversarial Training: Following the pre-training phase, the UNet-based discriminator was introduced, and the full model was trained end-to-end. In this phase, the generator was optimized using a composite loss function, combining the pixel-wise L1 loss with the adversarial loss. The learning rate was initialized at $2x10^{-4}$ and was subject to a step decay schedule, being halved every 20 epochs to allow for finer adjustments as the model approached convergence.

2.3 image analysis

2.3.1 Objective image quality evaluation

The quality of generated image was evaluated objectively using the following metrics: peak signal-to-noise ratio (PSNR), structure similarity index measurement (SSIM). Each criterion was calculated between enhanced and standard images. Higher PSNR or SSIM indicates better image quality and lower noise level.

$$\mathrm{PSNR} = 10 \cdot \log_{10}\left(\frac{\mathrm{L}^2}{\mathrm{MSE}}\right), \quad \mathrm{MSE} = \frac{1}{\mathrm{N}}\sum_{\mathrm{i}=1}^{\mathrm{N}}(\mathrm{x_i} - \mathrm{y_i})^2$$

$$\mathrm{SSIM}(\mathrm{x}, \mathrm{y}) = \frac{(2\mu_{\mathrm{x}}\mu_{\mathrm{y}} + \mathrm{C}_1)(2\sigma_{\mathrm{xy}} + \mathrm{C}_2)}{(\mu_{\mathrm{x}}^2 + \mu_{\mathrm{y}}^2 + \mathrm{C}_1)(\sigma_{\mathrm{x}}^2 + \sigma_{\mathrm{y}}^2 + \mathrm{C}_2)}$$

Statistical comparisons between fast-scan and enhanced images were conducted using the Wilcoxon signed-rank test to determine the significant differences in PSNR, SSIM across different reconstruct methods (P value < 0.05 was considered statistic significant.)

2.3.2 Subjective image quality evaluation

All reconstructed images underwent a retrospective analysis by two independent, board-certified nuclear medicine physicians who were blinded to the image acquisition protocol (i.e., standard, fast-scan, or deep learning post-processed). The physicians evaluated the image quality based on three key metrics: overall image quality, lesion conspicuity, and diagnose confidence. A 5-point Likert scale was utilized for all ratings, with a score of 1 indicating poor quality and 5 representing excellent quality. Specific criterion were shown in Table 1.

Table 1
5-point Likert scale for image quality, lesion conspicuity, and image sharpness

Score	Overall image quality	Lesion Conspicuity	Diagnose confidence
1	Unacceptable image quality and nondiagnostic	Invisible and extremely difficult to identify	No diagnostic confidence; interpretation impossible due to severe image degradation.
2	Suboptimal image quality with impairment of diagnostic confidence	Difficult to identify but some details are recognizable	Low diagnostic confidence; major uncertainty in lesion detection or characterization.
3	Acceptable image quality and not affecting the diagnostic confidence	Moderate clarity, with most details identifiable	Moderate diagnostic confidence; sufficient for clinical interpretation despite minor uncertainty.
4	Good image quality and diagnostic confidence	Clearly visible, with details easily recognizable	High diagnostic confidence; clear lesion delineation with minimal ambiguity.
5	Excellent image quality and absolute diagnostic confidence	Extremely clear, with all details very easily identifiable	Absolute diagnostic confidence; unequivocal identification and characterization of all relevant findings.

2.4.4 Statistical Analysis

To ensure the robustness of the subjective ratings, inter-rater reliability was assessed using both the Pearson correlation coefficient, which measures the linear relationship between the two physicians' ratings, and Cohen's Kappa statistic, which evaluates agreement beyond chance. The interpretation of Cohen's Kappa values was as follows: ≥ 0.8 indicated almost perfect agreement, 0.6–0.8 substantial agreement, 0.4–0.6 moderate agreement, 0.2–0.4 fair agreement, and < 0.2 poor agreement.

To compare the different imaging models, the mean subjective scores were analyzed using the Wilcoxon signed-rank test to determine if there were significant differences ($P < 0.05$) among the various protocols and enhancement techniques. These comparisons were performed for the entire dataset and four subgroups.

The statistical analyses were conducted using Python version 3.8, leveraging the pandas, and scipy libraries.

Result

3.1 Objective Evaluation

Objective image quality metrics demonstrated a significant enhancement in images processed with the CDDU-GAN framework compared to the unprocessed fast-scan acquisitions. As detailed in Table 2, the application of the model yielded substantial improvements in both PSNR and SSIM. The performance gains were most pronounced for the PET/CT datasets, which are inherently characterized by higher levels of granular noise. Specifically, the average PSNR increased by 3.3 dB for the FPC cohort and 2.5 dB for the GaPC cohort. In contrast, the improvements for the PET/MR datasets were more moderate, with average PSNR gains of 0.9 dB for the FPM group and 0.2 dB for the GaPM group. These results indicate that the CDDU-GAN architecture is particularly effective at mitigating noise and restoring image fidelity in acquisitions with lower intrinsic signal-to-noise ratios.

Table 2
PSNR and SSIM analysis of fast scan and CDDU-GAN enhanced images

	PSNR			SSIM		
	Fast	**CDDU-GAN**	**P-value**	**Fast**	**CDDU-GAN**	**P-value**
FPC	40.9±2.9	44.2±2.8	0.002	0.967±0.015	0.983±0.008	0.002
FPM	41.5±6.4	42.4±6.5	0.001	0.963±0.038	0.969±0.033	0.001
GaPC	44.3±5.1	46.8±4.8	0.003	0.973±0.026	0.983±0.017	0.004
GaPM	53.9±4.2	54.1±3.3	0.330	0.997±0.002	0.998±0.001	0.0005
Total	46.8±7.5	48.2±6.6	< 0.0001	0.980±0.026	0.986±0.020	< 0.0001

3.2 Subjective image analysis

A high degree of consistency between the two reviewing physicians was confirmed prior to the primary subjective analysis. Pearson correlation coefficients demonstrated a strong positive linear relationship for overall image quality ($r = 0.953$), lesion clarity ($r = 0.950$), and diagnose confidence ($r = 0.925$), with all p-values being highly significant ($p < 0.0001$). Complementing this, Cohen's Kappa statistics indicated "almost perfect agreement" for overall image quality ($\kappa = 0.810$) and lesion clarity ($\kappa = 0.834$), and "substantial agreement" for diagnose confidence ($\kappa = 0.787$). These findings affirm the robustness and reproducibility of the subjective scoring methodology.

The subjective assessment, summarized in Table 3, revealed that the CDDU-GAN model provided a marked improvement in perceived image quality, restoring diagnostic utility to the rapid-acquisition scans. Across the entire study population, the mean scores for the unprocessed fast-scan images were significantly lower than both the CDDU-GAN-enhanced and the standard-dose images for all three metrics: overall image quality, lesion conspicuity, and diagnostic confidence ($p < 0.05$ for all comparisons).

The application of the CDDU-GAN algorithm significantly elevated these scores. For the total cohort, the mean diagnostic confidence score rose from 3.37 ± 1.27 for the fast-scan protocol to 3.78 ± 1.22 after enhancement. While the enhanced images did not uniformly achieve the quality of the standard protocol (mean diagnostic confidence: 4.22 ± 1.23), they consistently demonstrated a substantial recovery of diagnostic value. This trend was consistently observed across all four subgroups. For example, in the particularly challenging 68Ga-PSMA PET/CT (GaPC) cohort, the CDDU-GAN improved the mean diagnostic confidence score from 2.50 ± 1.07 (low confidence) to 3.22 ± 1.23 (moderate confidence), thereby restoring clinical utility to images that might otherwise have been deemed non-diagnostic.

Table 3
Comparative analysis of subjective image quality scores across different imaging protocols and cohorts.

	Imaging protocol	Overall image quality	Lesion Conspicuity	Diagnose confidence
FPC	fast	4.200 ± 1.600	4.200 ± 1.600	2.900 ± 1.446[a]
	CDDU-GAN	4.200 ± 1.600	4.200 ± 1.600	3.200 ± 1.661
	standard	4.600 ± 1.200	4.600 ± 1.200	3.600 ± 1.744
FPM	fast	4.571 ± 0.495	4.571 ± 0.495	4.071 ± 0.884[a]
	CDDU-GAN	4.571 ± 0.495	4.571 ± 0.495	4.286 ± 0.881
	standard	4.714 ± 0.452	4.714 ± 0.452	4.857 ± 0.350
GaPC	fast	3.000 ± 1.886	3.000 ± 1.886	2.500 ± 1.067[a,b]
	CDDU-GAN	3.667 ± 1.700	3.667 ± 1.700	3.222 ± 1.227[a]
	standard	3.667 ± 1.700	3.667 ± 1.700	3.833 ± 1.424
GaPM	fast	3.618 ± 0.728[b]	3.588 ± 0.732	3.824 ± 0.984[a,b]
	CDDU-GAN	4.059 ± 0.539	4.059 ± 0.539	4.206 ± 0.631[a]
	standard	4.176 ± 0.567	4.176 ± 0.567	4.529 ± 0.606
Total	fast	3.779 ± 1.367[a,b]	3.767 ± 1.370[a,b]	3.372 ± 1.267[a,b]
	CDDU-GAN	4.093 ± 1.197	4.093 ± 1.197	3.779 ± 1.224[a]
	standard	4.256 ± 1.112	4.256 ± 1.112	4.221 ± 1.233

◦ [a] Indicates a statistically significant difference ($p < 0.05$) compared to the standard-dose protocol within the same cohort.

◦ [b] Indicates a statistically significant difference ($p < 0.05$) compared to the CDDU-GAN enhanced protocol within the same cohort.

◦ Abbreviations: FPC, ^{18}F-PSMA PET/CT; FPM, ^{18}F-PSMA PET/MR; GaPC, ^{68}Ga-PSMA PET/CT; GaPM, ^{68}Ga-PSMA PET/MR.

3.3 Representative Case Analysis

Visual inspection of the reconstructed images confirms the quantitative and subjective improvements observed across the cohorts. Figure 2 illustrates a representative case of ^{18}F-PSMA(PET/CT (FPC) imaging. The 30s rapid-scan image (Fig. 2, left) is characterized by severe grainy noise and poor contrast-to-noise ratio, which significantly impairs the delineation of tracer uptake regions. After

processing with the CDDU-GAN framework, the noise is markedly suppressed while the structural details and focal uptake intensity are preserved (Fig. 2, middle), demonstrating a high degree of fidelity to the 120s standard-dose "ground truth" image (Fig. 2, right). This visual restoration directly supports the observed increase in diagnostic confidence scores, particularly in PET/CT cases where intrinsic noise levels are higher.

Discussion

This study demonstrates the successful application of a novel deep learning framework, CDDU-GAN, for the enhancement of rapid-acquisition 18F-PSMA and 68Ga-PSMA PET images obtained from both PET/CT and PET/MR systems. Our results confirm that this approach can significantly improve image quality, bridging the diagnostic gap between simulated low-count, fast-scan images and full-count, standard-dose images. The key finding is that the CDDU-GAN model not only enhances objective image metrics but also substantially improves subjective image quality and, most critically, restores the diagnostic confidence of clinicians, thereby supporting the feasibility of accelerated PSMA PET imaging protocols.

A central observation from our objective analysis was the differential performance of the CDDU-GAN across imaging modalities. The model yielded more substantial improvements in PSNR and SSIM for PET/CT data compared to PET/MR data. This is likely attributable to the intrinsically different noise characteristics and reconstruction algorithms of the two platforms. PET/CT images are often subject to higher levels of granular statistical noise, a domain where deep learning denoising algorithms have proven to be particularly effective. The dual-dense connections and channel attention mechanisms within our CDDU-GAN architecture are specifically designed to preserve fine textures and edges while suppressing noise, making the model highly adept at restoring the quality of these noisier PET/CT acquisitions. The more modest gains in PET/MR, which typically presents with lower noise and higher intrinsic contrast, suggest that while the model is still beneficial, the margin for improvement is narrower.

The subjective evaluations, which represent the clinical endpoint of this work, strongly corroborated the objective findings. The excellent inter-rater reliability, established through both Pearson correlation and Cohen's Kappa statistics, lends high credibility to the physician assessments. Across all cohorts, the CDDU-GAN-enhanced images were rated significantly higher than their unprocessed fast-scan counterparts in terms of overall quality, lesion conspicuity, and diagnostic confidence. For instance, in the GaPC cohort, the model elevated images from a level of low diagnostic confidence to one of moderate, clinically acceptable confidence. This transformation is pivotal, as it suggests that a four-fold reduction in scan time—from 120s to 30s per bed for PET/CT, and 240s to 60s for PET/MR—can be achieved without a critical loss of diagnostic information. Such an acceleration in workflow could translate to tangible benefits, including increased patient comfort, reduced motion artifacts, and substantially improved scanner throughput, which is a significant logistical and economic advantage for busy nuclear medicine departments.

Our study has several limitations that warrant consideration. First, the investigation was conducted at a single institution, and although it involved two different scanner types, the findings require validation in a larger, multi-center study to ensure the model's generalizability across different hardware vendors and imaging protocols. Second, the fast-scan data was generated by retrospectively subsampling listmode acquisitions. While this is a well-established and valid technique for simulating reduced-count acquisitions, it may not perfectly replicate the Poisson noise distribution and electronic noise characteristics of a true prospective short-duration scan. Third, while we systematically divided our cohorts for training and testing, with the entire GaPC cohort reserved for independent testing, the sample sizes for some subgroups were relatively small, which may limit the statistical power of certain sub-analyses. Finally, our evaluation focused on image quality and diagnostic confidence; we did not assess the impact of the framework on downstream quantitative metrics (e.g., SUV measurements) or its ultimate effect on clinical decision-making and patient outcomes.

Conclusion

Our study provides robust evidence that a deep learning-based image enhancement framework using a CDDU-GAN architecture can effectively restore the quality of four-fold accelerated PSMA PET images. The model significantly improves objective and subjective image quality, leading to a recovery of diagnostic confidence across different PSMA radiotracers and PET imaging platforms. This technology holds substantial promise for optimizing clinical workflows, making PSMA PET imaging faster, more efficient, and more comfortable for patients.

Abbreviations

PSMA
Prostate-Specific Membrane Antigen
CDDU-GAN
Channel Dense Dense U-Generative Adversarial Network
PET
Positron Emission Tomography
CT
Computed Tomography
MR
Magnetic Resonance
PSNR
Peak Signal-to-Noise Ratio
SSIM
Structural Similarity Index
FPC
18F-PSMA PET-CT
FPM

18F-PSMA PET-MR
GaPC
68Ga-PSMA PET-CT
GaPM
68Ga-PSMA PET-MR

Declarations

Ethics approval and consent to participate This prospective study was approved by the Institutional Review Board of Shanghai Changhai Hospital in accordance with the Declaration of Helsinki. Written informed consent was obtained from all individual participants included in the study.

Consent for publication Consent for publication was obtained from the patient(s) for the images presented in this article.

Availability of data and materials The datasets generated and/or analysed during the current study are not publicly available due to patient privacy restrictions but are available from the corresponding author on reasonable request.

Competing interests The authors declare that they have no competing interests.

Funding This work was supported by the Xiamen Natural Science Foundation Project (Grant No. 3502Z202373090 to NG), the Major Research Plan of National Natural Science Foundation of China (Key Programme) (Grant No. 92359204 to CZ), the Explorers Program of Shanghai (Basic Research Funding) (Grant No. 25TS1406400 to CZ), and the Shanghai Hospital Development Center (Grant No. SHDC12023103 to CZ).

Authors' contributions CC and BP contributed equally to this work. CC and CZ conceived the clinical study. BP and NG designed the CDDU-GAN algorithm. ZG, QY, GP, and SL performed data acquisition and clinical subjective image analysis. LZ and LX contributed to data processing and software optimization. CC and BP drafted the manuscript. NG and CZ supervised the project, secured funding, and critically revised the manuscript. All authors read and approved the final manuscript.

Acknowledgements Not applicable.

Authors' information Not applicable.

References

1. Hofman MS, et al. Prostate-specific Membrane Antigen PET: Clinical Utility in Prostate Cancer, Normal Patterns, Pearls, and Pitfalls. Radiographics. 2018;38(1):200–17.
2. Oh SW, Cheon GJ. Prostate-Specific Membrane Antigen PET Imaging in Prostate Cancer: Opportunities and Challenges. Korean J Radiol. 2018;19(5):819–31.

3. Eiber M, Fendler WP, Rowe SP, Calais J, Hofman MS, Maurer T, et al. Prostate-Specific Membrane Antigen Ligands for Imaging and Therapy. J Nucl Med. 2017;58(Suppl 2):S67–76.
4. Schwarzenboeck SM, Rauscher I, Bluemel C, Fendler WP, Rowe SP, Pomper MG, et al. PSMA Ligands for PET Imaging of Prostate Cancer. J Nucl Med. 2017;58(10):1545–52.
5. Vetrone L, Fortunati E, Castellucci P, Fanti S. Future Imaging of Prostate Cancer: Do We Need More Than PSMA PET/CT? Semin Nucl Med. 2024;54(1):150–62.
6. Huang S, Ong S, McKenzie D, Mirabelli A, Chen DC, Chengodu T, et al. Comparison of 18F-based PSMA radiotracers with [68Ga]Ga-PSMA-11 in PET/CT imaging of prostate cancer—a systematic review and meta-analysis. Prostate Cancer Prostatic Dis. 2023;27(4):654–64.
7. Domachevsky L, Bernstine H, Goldberg N, Nidam M, Catalano OA, Groshar D. Comparison between pelvic PSMA-PET/MR and whole-body PSMA-PET/CT for the initial evaluation of prostate cancer: a proof of concept study. Eur Radiol. 2020;30(1):328–36.
8. Jentjens S, Mai C, Ahmadi Bidakhvidi N, De Coster L, Mertens N, Koole M, et al. Prospective comparison of simultaneous [68Ga]Ga-PSMA-11 PET/MR versus PET/CT in patients with biochemically recurrent prostate cancer. Eur Radiol. 2022;32(2):901–11.
9. Jimenez-Mesa C, Arco JE, Martinez-Murcia FJ, Suckling J, Ramirez J, Gorriz JM. Applications of machine learning and deep learning in SPECT and PET imaging: General overview, challenges and future prospects. Pharmacol Res. 2023;197:106984.
10. Munoz C, Ellis S, Nekolla SG, Kunze KP, Vitadello T, Neji R, et al. MRI-Guided Motion-Corrected PET Image Reconstruction for Cardiac PET/MRI. J Nucl Med. 2021;62(12):1768–74.
11. Deller TW, Mathew NK, Hurley SA, Bobb CM, McMillan AB. PET Image Quality Improvement for Simultaneous PET/MRI with a Lightweight MRI Surface Coil. Radiology. 2021;298(1):166–72.
12. Messerli M, et al. Impact of a Bayesian penalized likelihood reconstruction algorithm on image quality in novel digital PET/CT: clinical implications for the assessment of lung tumors. EJNMMI Phys. 2018;5(1):27.
13. Witkowska-Patena E, et al. Ordered subset expectation maximisation vs Bayesian penalised likelihood reconstruction algorithm in 18F-PSMA-1007 PET/CT. Ann Nucl Med. 2020;34(3):192–9.
14. Sadeghi F, et al. Phantom and clinical evaluation of Block Sequential Regularized Expectation Maximization (BSREM) reconstruction algorithm in 68Ga-PSMA PET-CT studies. Phys Eng Sci Med. 2023;46(3):1297–308.
15. Pozaruk A, et al. Augmented deep learning model for improved quantitative accuracy of MR-based PET attenuation correction in PSMA PET-MRI prostate imaging. Eur J Nucl Med Mol Imaging. 2021;48(1):9–20.
16. Mostafapour S, et al. Feasibility of Deep Learning-Guided Attenuation and Scatter Correction of Whole-Body 68Ga-PSMA PET Studies in the Image Domain. Clin Nucl Med. 2021;46(8):609–15.
17. Hosch R, Weber M, Sraieb M, et al. Artificial intelligence guided enhancement of digital PET: scans as fast as CT? Eur J Nucl Med Mol Imaging. 2022;49(13):4503–15.

18. Dutta K, Laforest R, Luo J, et al. Deep learning generation of preclinical positron emission tomography (PET) images from low-count PET with task-based performance assessment. Med Phys. 2024;51(6):4324–39.
19. Kaviani S, Sanaat A, Mokri M, et al. Image reconstruction using UNET-transformer network for fast and low-dose PET scans. Comput Med Imaging Graph. 2023;110:102315.
20. Sanaat A, Shiri I, Arabi H, et al. Deep learning-assisted ultra-fast/low-dose whole-body PET/CT imaging. Eur J Nucl Med Mol Imaging. 2021;48:2405–15.
21. Pan S, Abouei E, Peng J, et al. Full-dose whole-body PET synthesis from low-dose PET using high-efficiency denoising diffusion probabilistic model: PET consistency model. Med Phys. 2024;51(8):5468–78.
22. Katsari K, Penna D, Arena V, et al. Artificial intelligence for reduced dose 18F-FDG PET examinations: a real-world deployment through a standardized framework and business case assessment. EJNMMI Phys. 2021;8(1):25.
23. Deng F, et al. Low-Dose 68Ga-PSMA Prostate PET/MRI Imaging Using Deep Learning Based on MRI Priors. Front Oncol. 2022;11:782587.
24. Zhao Y, et al. Deep Supervised Residual U-Net for Automatic Characterization of Lesions on 68Ga-PSMA PET/CT images. J Nucl Med. 2019;60(suppl 1):1217.
25. Jia F, Wong WH, Zeng T, DDUNet. Dense Dense U-Net with Applications in Image Denoising. In: 2021 IEEE/CVF International Conference on Computer Vision Workshops (ICCVW); 2021; Montreal, BC, Canada. pp. 354–364.

Figures

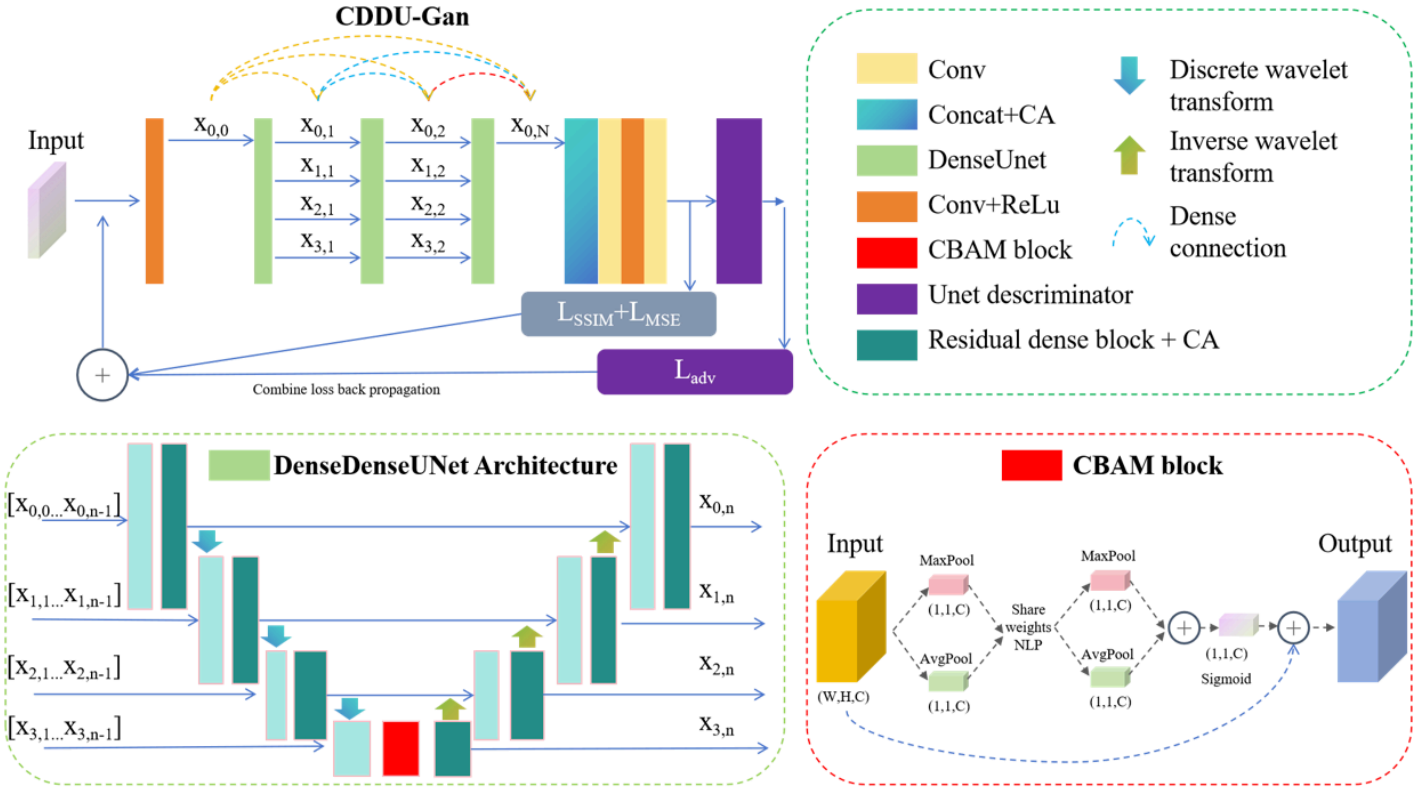


Figure 1

Channel Dense Dense U-GAN(CDDU-GAN), including (A) the structure of the CDDU-Gan network, (B) the structure of Dense Dense Unet, (C) the structure of CBAM block.

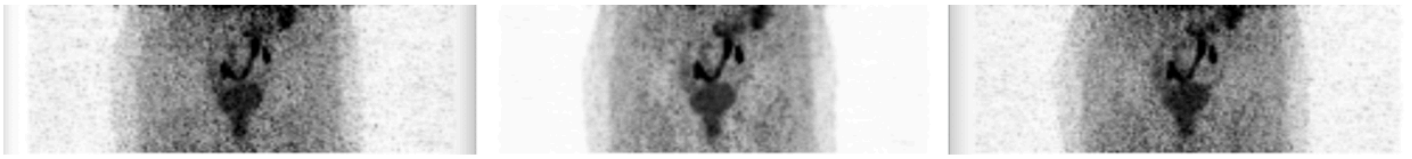


Figure 2

Comparison between fast PSMA imaging, algorithm processing results and standard MIP images. The left is 30s FPC imaging, the middle is the result of algorithm processing, and the right is the standard 120s scanning image.